J Mater Sci (2023) 58:11631–11646

Composites & nanocomposites

Construction and performance of composite nanoporous PVDF membrane loaded with TiO_2-based catalysts for organic pollutants' removal

Peihang Li[1], Hongshun Ran[1], Yaoyu Pan[1], Ziqiang Xu[2], Xueqin Chen[2,3,*], Cao Li[1,2], and Bingbing Jiang[1,2,*]

[1] Key Laboratory of Polymer Material in Hubei Province, Hubei University, Wuhan 430062, China
[2] Key Laboratory of Green Preparation and Application for Functional Materials, Ministry of Education, Hubei University, Wuhan 430062, China
[3] Department of Polymer, School of Material Science and Engineering, Hubei University, Wuhan 430062, Hubei, China

Received: 11 April 2023
Accepted: 29 June 2023
Published online: 13 July 2023

ABSTRACT

Membrane separation is one of the most effective ways to remove organic dyes in wastewater. Rationally regulating the pore size of separation membranes would contribute to great performance. However, membranes with a uniform pore structure make it difficult to simultaneously realize high flux and excellent rejection ratio. Herein, functional composite nanoporous fiber membrane material with visible-light-driven self-cleaning performance was constructed by spinning hypercrosslinked polystyrene nanoparticles (HCPNPs) and TiO_2-based catalysts into the electrospun membrane of polyvinylidene fluoride (PVDF). The composited fiber membrane with a hierarchical pore structure exhibits unique performances: excellent adsorption capacity for organic dyes, reaching 12 $mg{\cdot}g^{-1}$ (methylene blue), respectively, extraordinary high photocatalytic degradation rate (up to 99%) and gorgeous cycle degradation performance for MB (degradation rate is maintained at 95% after five cycles), and excellent comprehensive performance for the removal of extensive pollutant library including organic dye, and antibiotic pollutant. Therefore, coupled with facile and economical synthesis, we provide a novel idea for advanced membrane construction, which has the potential to be widely used for organic pollutants' removal in sewage treatment.

Handling Editor: Chris Cornelius.

Address correspondence to E-mail: 20120073@hubu.edu.cn; bingbingjiang@hubu.edu.cn

https://doi.org/10.1007/s10853-023-08738-3

GRAPHICAL ABSTRACT

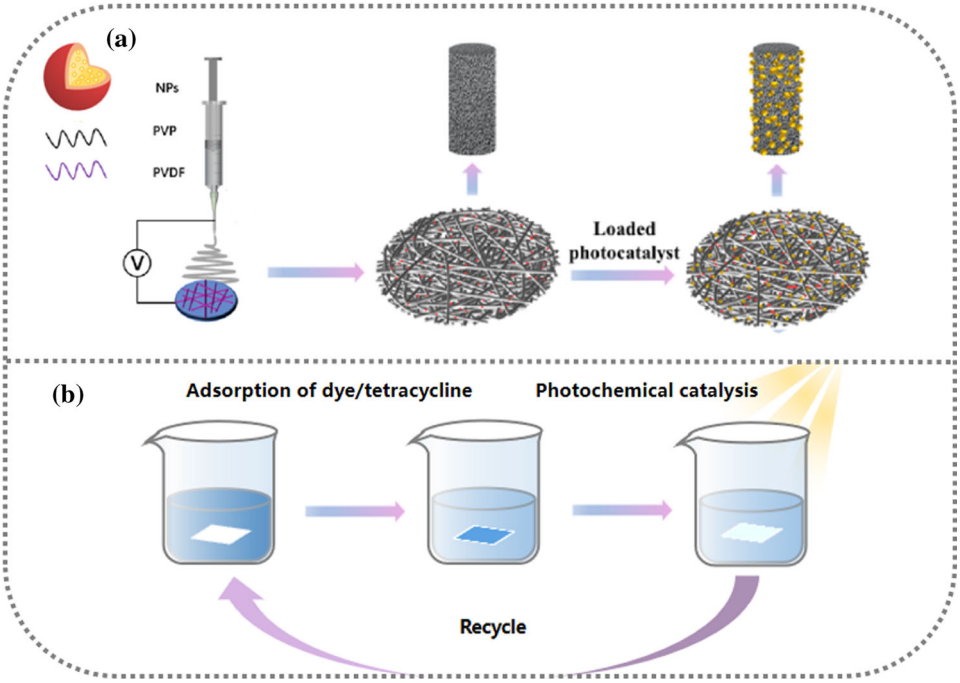

Introduction

In recent years, water contamination by dye discharges from various industries (e.g., paper making, textile dyeing, cosmetics, etc.) has attracted more and more attention due to their toxic effects on humans and aquatic organisms [1]. The dye contaminants in water are toxic and carcinogenic. Therefore, it is necessary to purify the dye pollutants. Many traditional technologies have been widely used to remove dyes from polluted water, including coagulation, flocculation, sedimentation, photocatalytic degradation, biological oxidation, ion exchange, and adsorption [2–6]. Adsorption is considered the best choice, due to its low cost, easy regeneration, and effectiveness. Various adsorption materials, such as activated carbon, zeolite, polymer silicate, and clay, have been used to remove organic dye pollutants [7, 8]. However, this powder or granular adsorption material has defects, such as the inability to be used on a large scale or being difficult to recycle. Membrane adsorption materials can significantly solve this problem.

Membrane adsorption technology is often used in water treatment processes. This technology can release the target material in the liquid when the external driving or the partial molar potential energy is inconsistent, and realize the screening, purification, and refinement of specific components in the mixture [9, 10]. There are many ways to synthesize membrane materials for membrane separation, including solution growth [11], chemical vapor deposition (CVD) [12], template synthesis [13], and electrospinning. Electrospinning technology possesses the advantages of easy synthesis and controllable membrane size [14]. The membrane material synthesized by electrospinning technology has a high specific surface area and rich pore structure, which has certain advantages in dye adsorption, cleaning oil leakage, and photocatalytic water purification [15, 16]. However, membranes with a uniform pore structure make it difficult to simultaneously achieve high flux and an excellent rejection ratio. The pore size distribution of pure fiber membrane is mainly concentrated at the micron level (belonging to the macroporous structure) [17], so it is hard to maintain high rejection of small molecules in

the mixture. To overcome these problems, nanoparticles with the microporous and mesoporous structures were mixed into the spinning membrane to make the composite membrane form a variety of pore structures. The macroporous structure of the fiber membrane can ensure a high flow rate, while the microporous and mesoporous structure brought by nanoparticles can improve the rejection of dye. This method of combining multiple organic compounds to make the polymer–matrix composites have extraordinary properties has been proved by research [18].

Meanwhile, during the membrane separation process, pollutants can be deposited between the pores of the membrane, which subsequently causes a series of problems, such as the reduction of membrane permeability and available time, the increase of loss as well as the excess of secondary treatment cost [19, 20].Ultimately, it might cause the filter membrane to fail. Therefore, advanced membrane with the ability to eliminate pollutants in situ is urgently required.

Photocatalytic technology has been proven to have high application value in eliminating organic pollutants and sterilization [21]. There are many types of photocatalysts, including titanium dioxide (TiO_2) [22], zinc oxide (ZnO) [23], zirconium dioxide (ZrO_2) [24], etc. Among various catalysts, titanium catalysts have been widely utilized, due to their low cost, high stability, and easy doping modification [25]. The synthesis methods of titanium-based photocatalysts usually include the hydrothermal method [26] and the solvothermal method [27]. In this study, the photocatalysts were synthesized by the one-step hydrothermal method [28, 29], because the photocatalysts synthesized by the hydrothermal method have good dispersion and high purity [30]. However, direct dispersion of photocatalysts in water is not easy to collect and reuse. The one-time damage rate is high, and it is also prone to re-pollution [31, 32]. Therefore, loading photocatalysts on the membrane can solve the above problems. Since the composite membrane can enrich pollutants firstly and then in situ catalytic degradation, it can be reused and has potential application value [33, 34].

In this study, electrospinning technology was employed to construct a PVDF-based composite fiber membranes by blending nanoparticles with the spinning solutions. Polyvinylidene fluoride (PVDF) is a commercially mature material of electrospinning membrane due to the outstanding chemical resistance, high thermal stability and membrane forming properties. Fiber membrane of polyvinylidene fluoride (PVDF) has been widely adopted for water treatment [35, 36]. Nanoparticles (NPs) with hypercrosslinked structure were synthesized using polystyrene (PS) and poly (tert-butyl acrylate)-polystyrene (PtBA-b-PS) diblocks as main building units. TiO_2-based catalysts with photocatalytic properties were synthesized via a one-pot hydrothermal method. PVDF was used as the fiber membrane substrate in this experiment, and polyvinyl pyrrolidone (PVP) was added at the early stage of membrane preparation and removed in the later stage to achieve the effective pore fabrication. The fibers showed rough, porous morphology so that when pollutants were adsorbed, uneven surfaces could intercept more substances, and light could also be more easily contacted with the interior, thereby improving the degradation efficiency of the photocatalytic process [37]. As shown in Scheme 1, the nanoparticles were mixed with PVDF and PVP to form the spinning solution. The large-scale fiber membrane materials were synthesized by electrospinning technology. Then the prepared photocatalyst was loaded on the fiber membrane to create the final composite membrane. Compared with pure PVDF fiber membrane, the introduction of nanoparticles makes the fiber membrane have a multi-stage pore structure, resulting in the higher adsorption and rejection ratio of dyes by the membrane. Expectant photocatalytic degradation performance after adsorption was achieved, due to the photocatalyst loading on the membrane. In addition, tetracycline is one of widely used antibiotics, its residue in water can lead to serious environmental problems, including ecological and human health damages [38]. Therefore, the performance of tetracycline degradation was also explored, to prove that the photocatalyst can not only degrade dyes, but also degrade other organic matter, which reflects the application diversity of the fiber membrane.

Experimental

Chemicals

Styrene (St), tert-butyl acrylate (tBA), poly(vinylidene fluoride) (PVDF, Mw = 400,000), polyvinyl pyrrolidone (PVP, Mw = 100,000), ethanol absolute, N, N-dimethylformamide (DMF), titanium oxysulfate,

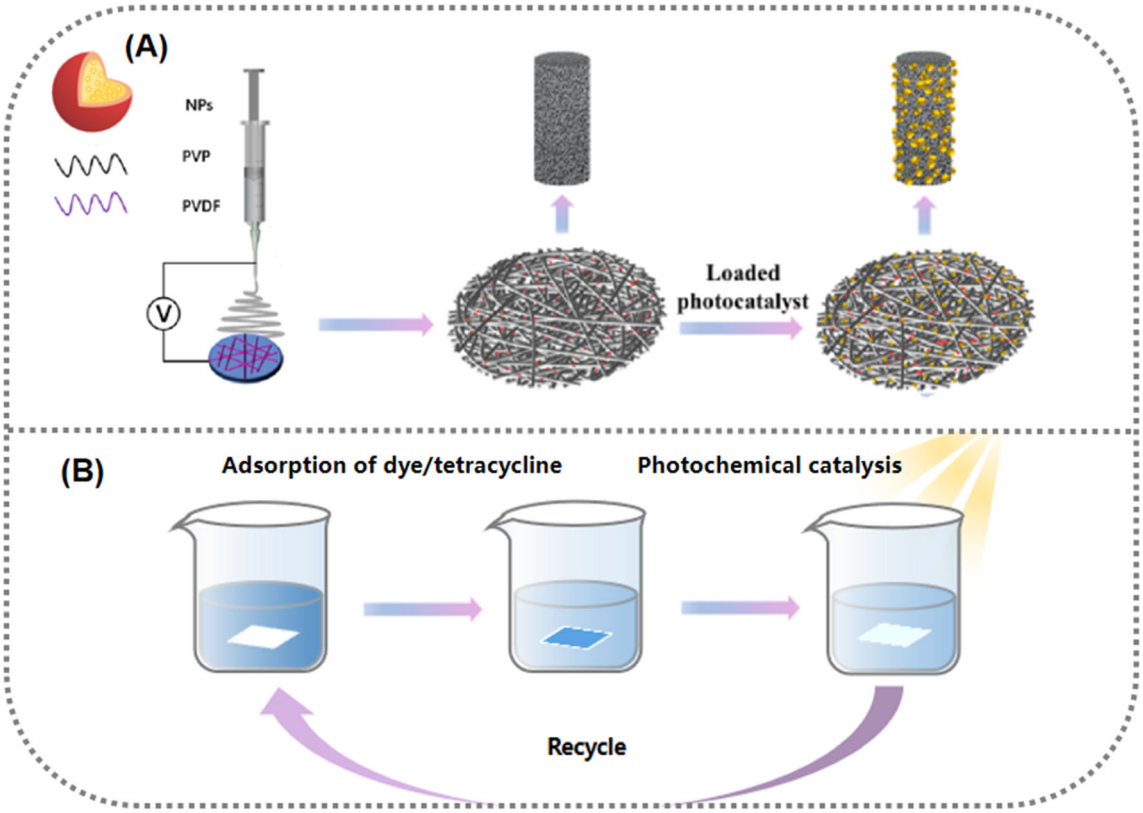

Scheme 1 The preparation of PVDF-based composite fiber membrane. **A** The electrospinning of PVDF/PVP-NPs suspension and loading photocatalyst on the membrane; **B** adsorption and photocatalytic degradation of dyes and tetracycline.

sodium metavanadate, and carbamide were purchased from Aladdin Reagent Co., Ltd 9 (Shanghai, China). 1,2-dichloroethane (1,2-DCE), ferric chloride anhydrous ($FeCl_3$), and silver nitrate were purchased from Sinopharm Chemical Reagent Co., Ltd. (China). Polystyrene (PS, Mw = 192,000) was purchased from Sigma Chemical Co., Ltd (USA).

Synthesis of nanoparticles (NPs)

Nanoparticles were synthesized by PS and PtBA-b-PS diblock synthesized in our previous work. (More detailed data and explanations on nanoparticles are reflected in previous work) [39]. The prepared diblock and PS were mixed with a 1,2-DCE ratio of 1: 9 and stirred at room temperature for 12 h to completely dissolve it. The $FeCl_3$ catalyst was weighed and transferred to a water bath at 40 °C for 48 h by magnetic stirring. Centrifugal washing with 1,2-dichloroethane, methanol, and deionized water was done after the reaction. After washing thoroughly, the product was dried in a vacuum at 25 °C for 24 h to obtain porous nanoparticles (NPs).

Synthesis of photocatalysts

Pure TiO_2 and different metal-doped catalysts were synthesized by the one-pot hydrothermal method [28, 29]. According to the difference in doped metal elements, the catalysts were named TiO_2, AgT, VT, and AgVT, respectively. The mass of each inorganic photocatalyst is fixed, and the content of doped metal elements is changed. The appropriate amount of $AgNO_3$, $NaVO_3{\cdot}2H_2O$, and other doped precursors was mixed with $TiOSO_4$ and $CO(NH)_2$ and then dissolved in distilled water. After stirring and homogenizing, the above products were put into 100 ml PTFE lining for subsequent hydrothermal steps. The reaction temperature was 150 °C, and the reaction time was ten h. When the temperature dropped to 25 °C, the residue was obtained from the product by high-speed centrifuge, washed with deionized water, and finally dried in a vacuum dryer at 40 °C to obtain AgVT, VT, and AgT which were different in the precursor, and the steps were the same. At the same time, TiO_2 is directly synthesized

without precursor, and the subsequent actions were also consistent with the previous steps.

Preparation of composite fiber membrane

PVDF/PVP composite fiber membrane was prepared by electrospinning [35, 40]. PVDF (wt %): PVP (wt %) = 2: 1 solid powder was added into the flask, and then 15 ml DMF solvent was added for ultrasonic stirring and dissolution. After dissolution, the blended spinning solution was obtained. PVP in the blend solution was used as a pore-forming agent. The obtained spinning solution was mixed with the prepared NPs, and the mass ratio of the NPs to PVDF was 1: 1. Due to the small part of the organic nanoparticles' reunion, the uniform spinning solution was obtained by ultrasonic dispersion after mixing. After fully dissolved, 5 ml of spinning solution was placed in a 5-ml syringe to fabricate polyurea fibers by the electrospinning equipment. The pushing rate of the needle speed of syringe was 2 ml·h^{-1}, respectively. The nanofibers were collected by a rolling collector (rotation rate of 100 r·min^{-1}) with a collecting distance of 20 cm between collector and electrode. The applying voltage was 25 kV. Finally, porous PVDF/PVP-NPs fiber was obtained, and the membrane of unblended nanoparticles prepared by the same method is called PVDF/PVP. The obtained mixed fiber membrane was placed in anhydrous ethanol for one hour. Then the new anhydrous ethanol was replaced and soaked in a constant temperature at 60 °C for 24 h to remove the PVP component from the fiber. Furthermore, a pure PVDF spinning solution without PVP was also prepared for comparison, labeled as PVDF. Finally, the pore-forming fiber is put into the vacuum drying oven for drying. 25 mg inorganic photocatalyst was transferred to 20 mL DMF and dispersed uniformly by ultrasound. The prepared fiber membrane was cut into a 5 × 5 cm fiber membrane and fixed on the receiving plate of the spinning machine. The positive and negative sides of the fiber membrane were sprayed with a 10 ml electric jet, and the electric jet speed was set to 10 ml·h^{-1}. The collection distance between the collector and the electrode was set to 10 cm, and the applied voltage is maintained at 25 kV. After spraying, the fiber membrane was removed and wrapped with tin foil to avoid light and then vacuum dried at 40 °C for 12 h. The obtained composite fiber membranes loaded with catalysts were named TiO_2-PVDF/PVP-NPs, AgT-PVDF/PVP-NPs, VT-PVDF/PVP-NPs, AgVT-PVDF/PVP-NPs.

Characterization methods

The morphology of nanoparticles, photocatalysts, and membranes was characterized by field emission scanning electron microscope (FESEM) from JEOL of Japan and transmission electron microscope (TEM; Tecnai G20, FEI, USA). To observe the cross-sectional morphology, the membrane was cryogenically fractured in liquid nitrogen. Before SEM characterization, the membrane surface was sputter-coated with a gold layer, and the characterization was carried out at an accelerating voltage of 3.0 kV. Chemical composition was analyzed by Fourier transform infrared (FTIR) from Thermo Fisher of USA, X-ray photoelectron spectroscopy (XPS, Thermo scientific ESC Alab 250xi, USA), energy-dispersive spectroscopy (EDS) on FESEM instrument, and thermogravimetric analysis (TGA, Mettler-Toledo, TGA/DSC 1/1100). The structure of photocatalysts was characterized by X-ray diffraction (XRD, Bruker D8 ADVANCE) and ultraviolet spectrophotometer (SHIMADZU, UV-3600, Japan). Surface areas of all the samples were calculated by the Brunauer–Emmett–Teller (BET) method and Barrett–Joyner–Halenda (BJH) approach (MIC-2460, USA). Concentration of dye in solution was characterized by ultraviolet spectrophotometer (SHIMADZU, UV-3600, Japan).

The methylene blue dye (MB) was used as a model dye to assess the adsorption and photocatalytic degradation ability of all the prepared samples under the visible light irradiation. The chemical structure of methylene blue dye (MB) is illustrated in Scheme. S1. Adsorption tests were conducted in 250-ml beaker with 1.0 g fiber membrane. The membrane was dipped with 100 ml of methylene blue (MB) dye solution of initial dye concentrations (10 mg/L). The dye solution was stirred on magnetic stirrer at 100 rpm (25 °C) to achieve equilibrium. At equilibrium, the concentration of MB was measured at λ_{max} 664 nm using ultraviolet spectrophotometer. The adsorption capacity of membrane was calculated by the following equation:

$$q_{\text{sorption}}\ (\text{mg/g}) = \frac{V(C_i - C_f)}{M}$$

In the formula, V is volume of dye solution (L), M is mass of adsorbent membrane used (g), C_f is final concentration of MB (mg/L), and C_i is initial concentration of MB (mg/L).

The appropriate amount of tetracycline hydrochloride solid was dissolved in deionized water, and the concentration of tetracycline solution was 10 mg·L^{-1}. Different fiber membranes were cut to the exact size and transferred to the same size of the surface vessel. 30 mL tetracycline solution was taken and put into the surface vessels, respectively, and then all the surface vessels were transferred to the photocatalytic device (the process needed to avoid light). Subsequently, the power supply was switched on, and the timer was turned on for light. Aliquots (1 ml) were withdrawn every 10 min. Finally, the fluid was tested by UV–visible spectrophotometer, scanning from 800 to 200 nm. Tetracycline will be degraded at the wavelength of 356 nm. The degradation rate (η, %) is calculated by the absorbance at this point. The formula is as follows:

$$\eta = \frac{C_t}{C_0} = \frac{A_t}{A_0} \times 100\%$$

C_0 is the mass concentration of tetracycline solution before photocatalytic degradation; C_t is the mass concentration of tetracycline solution after t hour degradation; A_0 is the absorbance of tetracycline solution at 356 nm before photocatalytic degradation; and A_t is the absorbance of tetracycline solution after photocatalytic degradation for t hours. For the cyclic degradation performance of the membranes, the collected membranes were washed with pure H_2O and methanol 3–4 times, respectively, until no absorbance could be detected in 356 nm and then dried before being reused in next cycle.

Results and discussion

Morphology and pore properties of nanoparticles

The morphology of nanoparticles (NPs) was observed by SEM measurements (Figure S1). Uniform spheric NPs are shown with the size about 150 nm. TEM image in Figure S1 (B) demonstrated lattice structure of NPs. These results present that the nanoparticles have uniform size and spherical morphology and mesoporous structure.

The nanoparticles show a high specific surface area up to 232.3 m^2·g^{-1} and the average pore size was 6.8 nm. As demonstrated in Figure S1 (C), the N_2 adsorption–desorption isotherm of nanoparticles displays the adsorption capacity of nitrogen increases rapidly with the increase of pressure at low pressure ($P/P_0 < 0.1$), indicating that there are a large number of micropore structures [41]. In the part of $0.3 < P/P_0 < 0.8$, the adsorption increment lags behind, which suggests that some mesoporous structures existed in the nanoparticles [42]. As shown in Figure S1 (D), the NPs present porous structures with the pore size in the range of 2–20 nm.

Morphology structure and photocatalytic performance of photocatalyst

The morphology of the synthesized samples was studied by transmission electron microscopy. The TEM images of TiO_2, $AgTiO_2$, $VTiO_2$, and $AgVTiO_2$ are shown in Figure S2(A-D). The particles are approximately spherical and evenly distributed. X-ray photoelectron spectroscopy confirmed the existence of doped atoms in the TiO_2 lattice. Figure S2(E–H) shows the peak values of each element in TiO_2, AgT, VT, and AgVT, respectively. Among them, the binding energy of Ti is shown at 480 eV (Figure S2 E), which can prove the successful synthesis of TiO_2 [43].The same peak is also observed in subsequent Figure S2 (F–H), which demonstrate the successful synthesis of TiO_2. The data in the form of black lines of dense wave lines are smoothed by the peak separation software to identify the absolute peak. The binding energies of Ag were shown on both sides of 370 eV in Figure S2 (FH), indicating that Ag was successfully doped into TiO_2 [44]. The binding energy of V appeared at about 520 eV (Figure S2 H), which proved the V element was successfully doped into TiO_2 [45].

The absorption in visible light and the effective separation of electrons and holes are crucial to photocatalytic activity. The effect of doping on the electronic band structure of TiO_2 was studied by UV–Vis absorption spectroscopy. It can be seen from Fig. 1a that doping changes the electronic band structure of TiO_2 and induces visible light absorption. The modification of the band structure will allow visible light photons to be absorbed, thus generating electron–

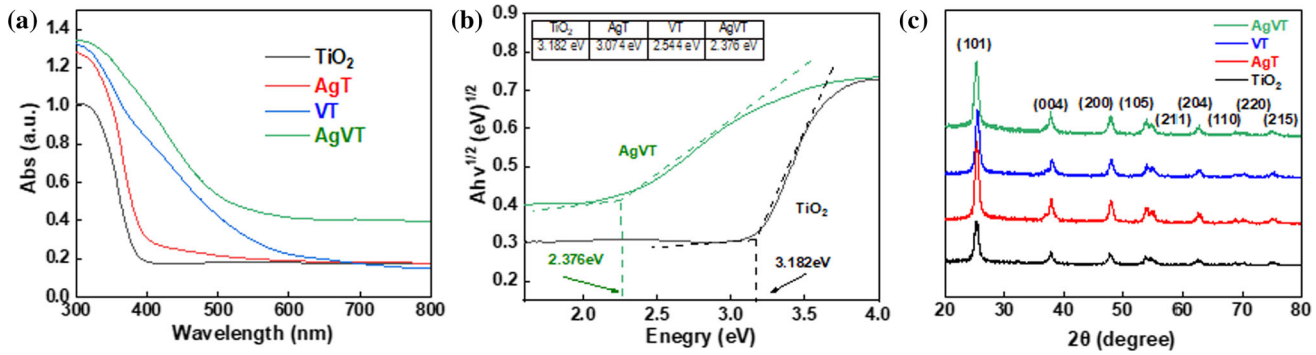

Figure 1 Photocatalysts doped with different metals: **a** UV–Vis diffuse reflectance spectroscopy; **b** Kubelka–Munk function graph; **c** XRD pattern.

hole pairs and improving the utilization of most solar spectra. Single metal element doping can induce the visible light absorption of TiO_2, and the visible light absorption is the most obvious in the co-doped samples of various metal elements. It is reported in the literature that doping V at the Ti site will introduce V three-dimensional state below the minimum conduction band, resulting in the decrease of the electronic band structure of TiO_2 [46]. The reduced band gap will absorb visible light photons and ultimately increasing the light activity [47]. Similarly, due to the modification of the band structure, Ag doping in TiO_2 also favors for the shifting of absorption edge to the visible area and successfully separate the electron–hole pairs [48]. Co-doping broadens the absorption range of TiO_2 in the visible light region, so the co-doping of Ag and V plays an essential role in the photocatalytic activity of visible light. The photodegradation response of AgV co-doped TiO_2 can be further improved by adjusting the doping concentration. Figure 1b shows that the band gaps of the four photocatalysts are TiO_2 (3.182 eV), AgT (3.074 eV), VT (2.544 eV), and AgVT (2.376 eV). Since the band gap of the AgVT sample is the smallest and the visible light absorption effect is the best, its solid visible light absorption makes the photocatalytic activity the best. Therefore, under visual light irradiation, the sample AgVT activated by visible light will produce more electron and hole pairs and participate in the photocatalytic redox reaction.

The X-ray diffraction patterns of the synthesized models are shown in Fig. 1c. The characteristic diffraction peaks of all samples are matched with those of pure anatase and show better photocatalytic activity under UV irradiation [49].

The photocatalytic activity of the prepared photocatalyst was evaluated by the catalytic degradation of methylene blue (MB) under the visible light. The photodegradation performance results are shown in Fig. 2. It illustrates the degradation activities of MB in the blank control group, TiO_2, AgT, VT, and AgVT, respectively. With the increase in illumination time, the MB content gradually decreased, and the characteristic absorption peak gradually shifted to the left in the lower wavelength direction, which may be related to the production of metabolites in the degradation process. Among them, the photocatalytic activity of AgVT was the strongest, attributing to the coupling of Ag and V in the TiO_2 lattice and the appropriate doping concentration. The photodegradation performance results are shown in Fig. 2f. C and C_0 represent the concentration and initial concentration of MB at a specific time, respectively. Doping improved the photocatalytic activity of TiO_2 under visible light irradiation, and all doped samples showed better activity than pure TiO_2.

Morphology and structure of composite membrane

Figure 3a demonstrates the thermal stability of various membranes. The weight loss ratio of pure PVDF/PVP fiber membranes is about 90%, and the fiber membrane with NPs will be slightly lower. This is because NPs are a kind of hypercrosslinked organic nanoparticles with good thermal stability. Additionally, the introduction of the photocatalyst also reduced the weight loss of the membrane.

The chemical structures of the composite membranes were analyzed by FTIR. In Fig. 3b, absorption peaks at 1401 and 1178 cm^{-1} were observed in every

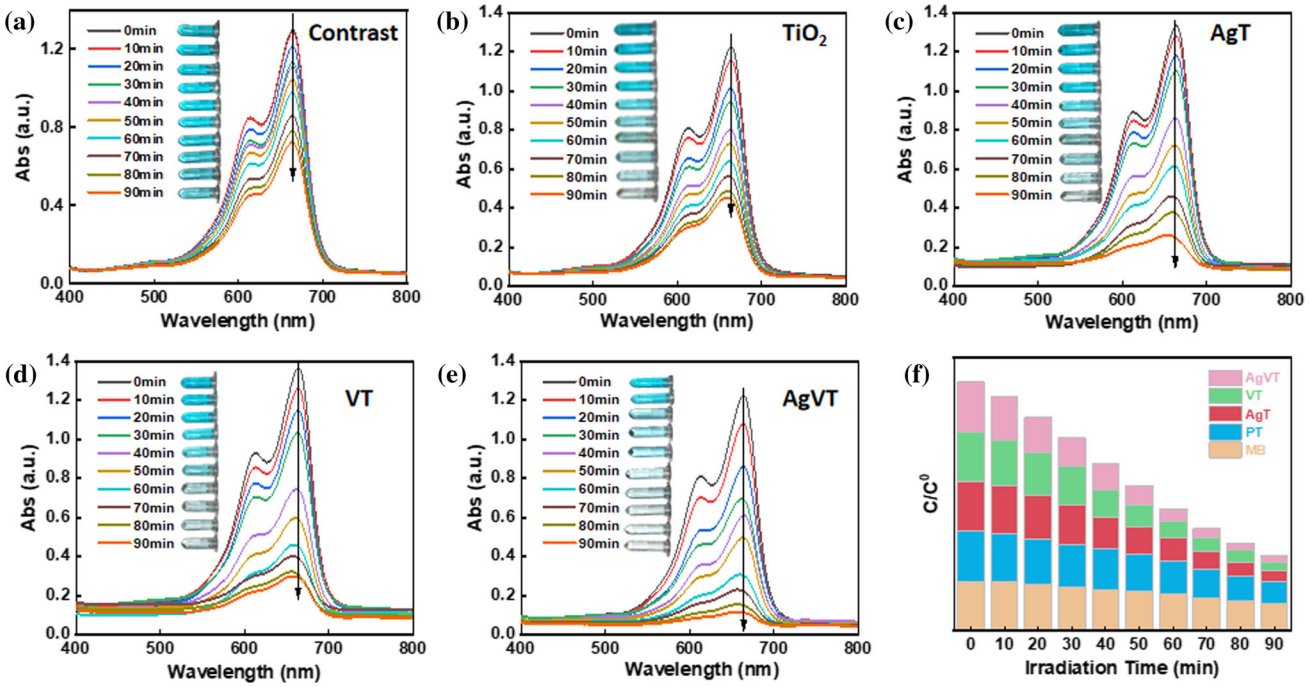

Figure 2 Different photocatalyst photocatalytic activity tests: **a** Blank control; **c** Pure TiO_2; **c** AgT; **d** VT; **e** AgVT; **f** Comparison of degradation efficiency.

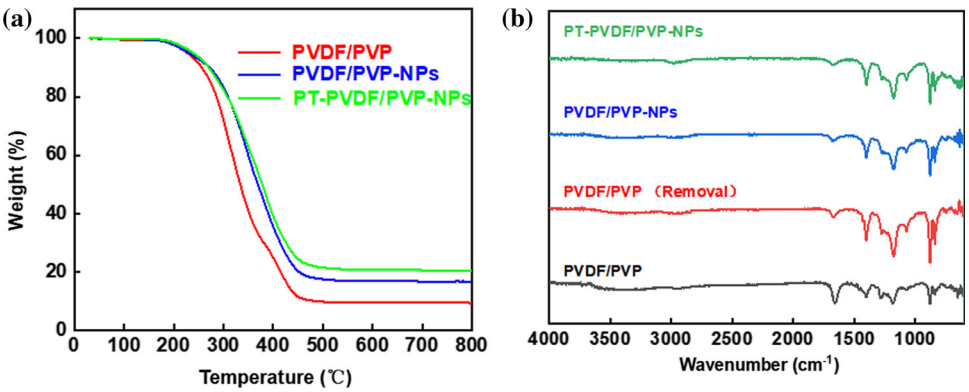

Figure 3 TG analysis (**a**) and the FT-IR spectrum (**b**) of different fiber membranes.

PVDF membrane, corresponding to the stretching vibration of $–CF_2$ and $–CH_2$. The characteristic peak near 1775 cm^{-1} should be attributed to polysubstituted benzene, which is caused by the introduction of NPs. This distinct absorption peak can be found in the fiber membrane containing NPs, which proves the successful introduction of organic nanoparticles. In addition, the distinct absorption peak of the carbonyl group (-C = O) of PVP polymer appeared at 1667 cm^{-1}. This distinct absorption peak was also evident in PVDF/PVP blend fiber. The intensity of this absorption peak in the fiber membrane after removing PVP was significantly reduced, which meant most of PVP components in the PVDF/PVP blend fiber were successfully removed during the pore formation process (Fig. 3b). In the infrared spectrum of PVDF-TiO_2 composite fiber membrane loaded with TiO_2, there was no characteristic peak inconsistent with that of the fiber membrane after pore-forming, which also indicated that the combination of TiO_2 did not form a new chemical bond in the fiber, but a physical load.

As shown in Fig. 4, the morphology of the PVDF-based fiber membrane before and after pore-forming was observed by SEM to determine whether the porous fiber membrane was successful. Figure 4a shows the micrograph of pure PVDF spinning film before pore-forming. It can be found that the overall

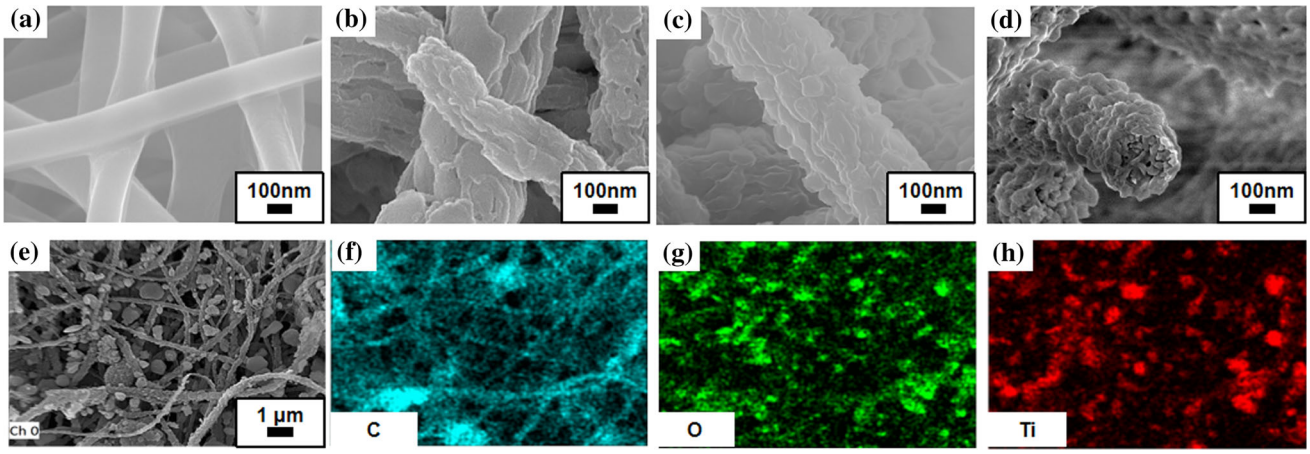

Figure 4 FESEM morphology observation of fiber membrane: **a** PVDF; **b** PVDF/PVP; **c** PVDF/PVP-NPs; **d** Cross-section of PVDF/PVP-NPs; **e** TiO_2-PVDF/PVP-NPs; EDS mapping element analysis of TiO_2-PVDF/PVP-NPs (**f**–**h**).

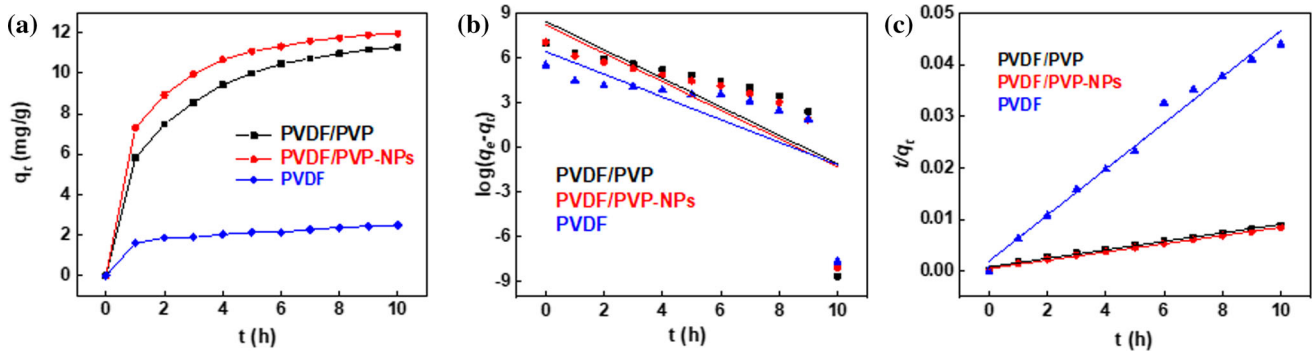

Figure 5 **a** The equilibrium adsorption amount of MB on different fiber membranes; The adsorption kinetics of MB on different fiber membranes **b** First-order kinetic adsorption; **c** Secondary kinetic adsorption.

fiber is very smooth and the average diameter of the fiber is less than 100 nm. Figure 4b is the microscopic image of the pore-forming process with PVP. It can be found that the surface of the fiber is very rough, and there are many synapses. This is because PVP required to be dissolved in the pore-forming process. When PVP is dissolved, some PVDF will be driven to overflow outward. To overcome the tension of the solvent, it will automatically curl up into spherical droplets. With the large amount of PVP dissolved, this rough fiber will eventually be formed. At this time, the overall diameter of the fiber decreased slightly and remained at about 90 nm, which was undoubtedly due to PVP dissolution. Figure 4c shows the fiber after adding NPs. After pore-forming, it was found that the diameter of the fiber increased slightly, owing to the certain amounts of NPs mixed into the fiber, and the overall diameter of the fiber reached about 200 nm. A very rough morphology could still be observed on the surface. To further verify the successful pore-forming of the fiber, not only the uneven surface but also the microscopic morphology of the fiber cross section was photographed by brittle fracture treatment. As shown in Fig. 4d, many c structures of the fiber can be observed at low magnification, and many small pore structures can be seen at high magnification. At the same time, the average pore size (calculated by the Brunauer–Emmett–Teller (BET) method and Barrett–Joyner–Halenda (BJH) approach (MIC-2460, USA)) of the membrane was determined to be 14.2 nm, which also confirmed the existence of microporous and mesoporous structures in the composite membranes. This indicates that the fiber has this hollow porous structure, which lays the foundation for subsequent adsorption experiments.

Figure 4e–h illustrates the morphology and the EDS mapping map of the inorganic photocatalyst

loaded on the fiber membrane. It shows in Fig. 4f–h that the Ti-based catalyst is uniformly dispersed in the fiber membrane, which will be of benefit for subsequent photocatalytic behaviors. The macropore structures of fiber membrane maintain very well in the composite membrane (Fig. 4e), and the roughness becomes more prominent which can improve the adhesion of organic dyes on the membrane, thereby promoting the industrial application of the composite membrane.

Dye adsorption performance

Figure 5a shows the adsorption of MB on fiber membranes with different porosity. It can be seen from the figure that the adsorption amount of MB on pure PVDF fiber membrane is meager, only about 2 $mg{\cdot}g^{-1}$. The adsorption of MB on the fiber membrane after pore-forming is significantly increased to about 10 $mg{\cdot}g^{-1}$. This is due to the successful pore-forming, the surface roughness increases, the pore structure increases, and the adsorption sites are rich. The adsorption capacity of nanofiber membrane with NPs was further increased to 12 $mg{\cdot}g^{-1}$, due to more pore structure provided by NPs, which was higher than that of other materials for organic dyes [50, 51]. This is also consistent with the previous SEM data.

Figure 5b, c shows two different kinetic model curves by fitting the adsorption data of PVDF, PVDF/PVP, and PVDF/PVP-NPs fiber membranes. Then by comparing the kinetic correlation coefficient (R^2) calculated by fitting to determine the fiber membrane in line with kinetic adsorption. The R^2 of the three kinds of fiber membranes in quasi-first-order fitting were 0.44592, 0.55148, and 0.49434, respectively; the R^2 of the three types of fiber membranes were 0.98385, 0.99516, and 0.98804, respectively. From the above data, the correlation coefficient (R^2) of the quasi-first-order kinetic adsorption model of the three kinds of fiber membranes was less than that of the quasi-second-order kinetic adsorption model (R^2). Through the comparison of these results, it can be seen that the PVDF/PVP-NPs composite fiber membrane follows the pseudo-second-order kinetic adsorption behavior in the adsorption process [52]. This proves that the fiber membrane is adsorbed by the diffusion of the target in the membrane, and the driving force of adsorption is the number of active sites on the surface of the adsorbent.

Photocatalytic degradation of MB with composited membranes

The absorbance of MB in the solution was measured by a UV spectrophotometer to determine the adsorption and photocatalytic degradation of MB on fiber membranes loaded with different catalysts. As shown in Fig. 6, the rate of each stage can be seen by comparing the photocatalytic degradation efficiency of MB with different photocatalyst-loaded composite fiber membranes. As shown in Fig. 6a, f, the composite membrane containing NPs has a faster adsorption rate and photocatalytic degradation efficiency when compared with the membrane without NPs. Figure 6b–e shows the rate comparison of TiO_2-PVDF/PVP-NPs, AgT-PVDF/PVP-NPs, VT-PVDF/PVP-NPs, AgVT-PVDF/PVP-NPs, and the four composite fiber membranes at each stage. It was also found that there was little difference in the rate of the fiber membrane supported by different catalysts. By recording the color change of the fiber membrane, it could be observed that the color of the fiber membrane after the adsorption saturation was dark blue, which was close to that of the MB solution. With the extension of the illumination time, the blue on the fiber membrane gradually became lighter. After 60 min of illumination, the color of the fiber membrane supported by all the photocatalysts could be restored to that before adsorption, which could prove that photocatalysis occurred on the membrane. Through the rate curve, it can also be found that in these composite fiber membranes, after reaching adsorption saturation, the photocatalytic irradiation for 200 min almost completely degrades remaining MB in the solution. Compared with other degradation solutions reported in the literature, the residual MB was excellent [53]. To better understand the photocatalytic ability of composite fiber membranes, the photocatalytic ability of the composite fiber membrane was compared with that of other membrane materials reported in the literature, and the results are shown in Table 1. This also indicates that this composite membrane has great application value in photocatalytic wastewater treatment.

Cyclicity of adsorption and photocatalytic degradation of MB

Considering the practical application environment of sewage treatment film, its recycling ability should also be investigated. As shown in Fig. 7, the cyclic

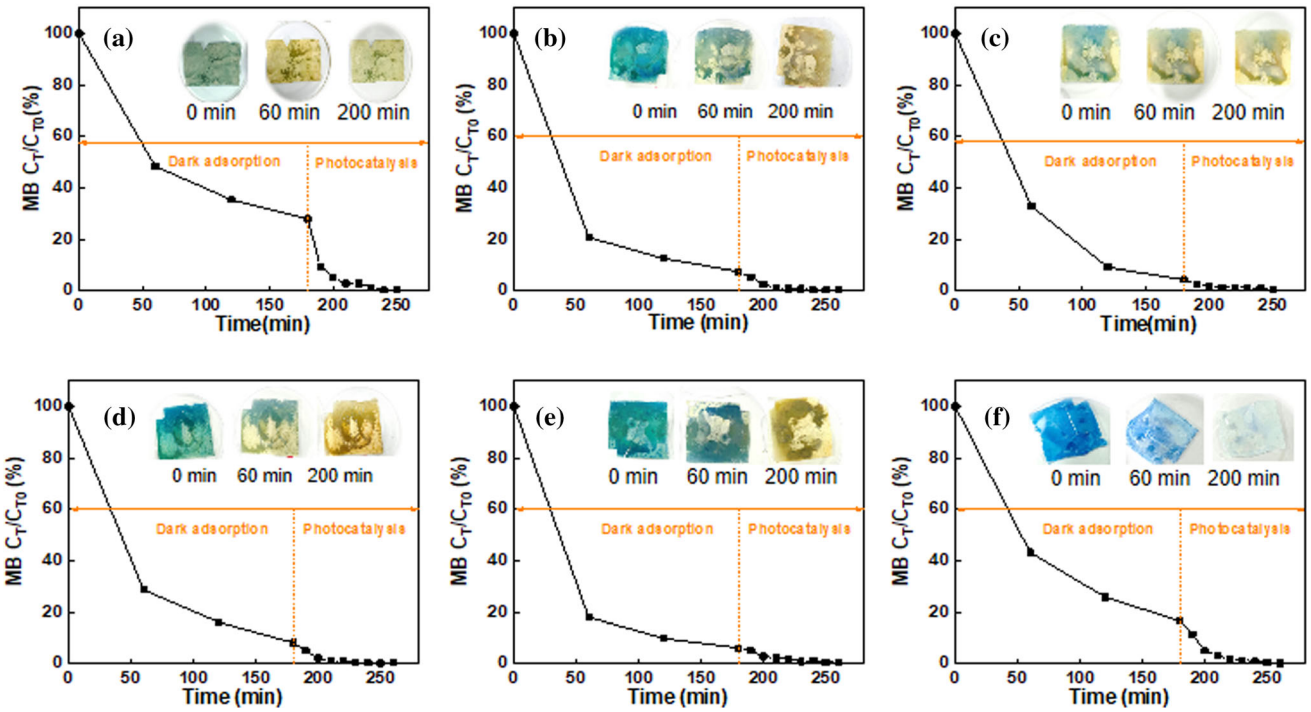

Figure 6 The photocatalytic degradation efficiency of MB by composite fiber membrane loaded with different photocatalysts **a** PVDF/PVP-NPs; **b** TiO_2-PVDF/PVP-NPs; **c** AgT-PVDF/PVP-NPs; **d** VT-PVDF/PVP-NPs; **e** AgVT-PVDF/PVP-NPs; **f** AgT-PVDF/PVP; Photographs corresponding to different films were as follows: adsorption MB reached saturation, photocatalytic time 60 min, photocatalytic time 200 min.

Table 1 Comparison of the photocatalytic capacities among composite membrane prepared in this work and reported in the literature

Photocatalyst/film substrate	Lights	Dye concentration	MB degradation rate (%)	Catalysis time (min)	Refs
TiO_2/glass hollow fiber	UV irradiation (wavelength 303 nm)	20 mg·L^{-1}	92.0	480	[54]
TiO_2/poly (vinyl alcohol-co-ethylene) Nanofibrous	UV irradiation (15 mW·cm^2)	10 mg·L^{-1}	97.3	150	[55]
ZnO/PVDF/GO	Xenon illumination (300 W)	10 mg·L^{-1}	86.8	100	[56]
TiO_2/Fe_2O_3 composite film	UV irradiation (400 W)	2×10^{-5} mol·L^{-1}	82.0	240	[57]
ZnO/PVDF	Visible Light (400 W)	10 mg·L^{-1}	96.3	360	[58]
TiO_2/borneol-based polymer	UV irradiation (wavelength 365 nm)	10 mg·L^{-1}	91.5	240	[59]
CdS/CMS/starch	Xenon illumination (350 W)	2×10^{-5} mol·L^{-1}	86.7	120	[60]
AgVT/PVDF	Visible Light (200 W)	10 mg·L^{-1}	99.0	200	Our work

adsorption and photocatalytic degradation of MB by the composite fiber membrane is demonstrated. Figure 7a shows the UV absorption spectra of residual MB in the solution after cyclic adsorption and photocatalysis. First, the solution was saturated in a dark environment and then subjected to continuous illumination for one hour. It can be found that with the increase in the number of cycles, the content of residual MB in the solution increased slightly at the same adsorption time, which is a normal phenomenon. After each illumination, the MB content can be reduced to a meager value, indicating that the

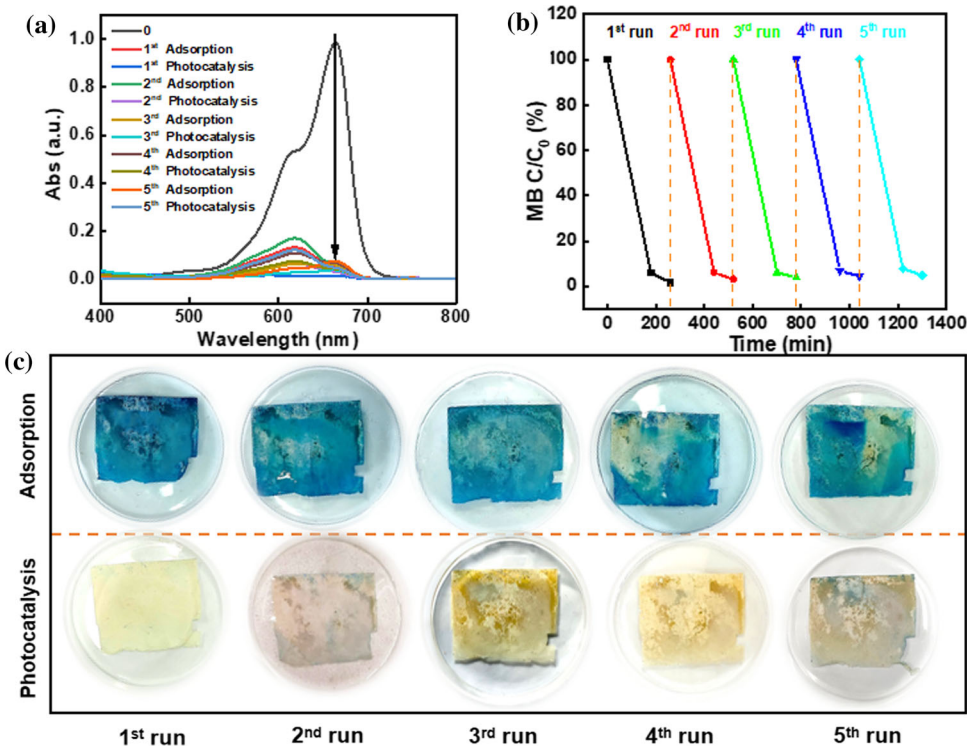

Figure 7 Cyclic adsorption and photocatalytic degradation of MB on composite fiber membranes: **a** Cyclic adsorption photocatalytic UV Spectra; **b** Degradation efficiency diagram of cyclic adsorption photocatalysis; **c** Color comparison before and after cyclic adsorption photocatalysis.

photocatalytic cycle effect is good. Figure 7b shows the comparison of degradation efficiency of cyclic adsorption photocatalysis. It can be seen from the figure that the cyclic photocatalytic ability of this kind of composite membrane is excellent. After five cycles, it maintains at a high adsorption value, and the adsorption ratio is as high as 95%. At the same time, the photocatalytic degradation rate of MB in the residual solution is also as high as 99% [54, 61]. It can be said that MB in the solution is almost completely degraded without residue. Figure 7c is the color comparison photograph of the composite membrane before and after cyclic adsorption photocatalysis. It can be found that the blue of the composite fiber membrane after adsorption saturation is deeper, the blue disappears after light degradation, and the color of the membrane is restored to the previous level. In addition, the color of the membrane after saturated adsorption in five cycles is still deeper, and the blue is also lighter after cyclic illumination, which can prove that its adsorption ability is still outstanding and the photocatalytic degradation performance is excellent.

Tetracycline degradation performance

The degradation ability of composite fiber membranes to the actual organic pollutants in the environment is also an important indicator of sewage treatment materials. Therefore, the absorbance of tetracycline solution with a particular concentration in the photocatalytic degradation of composite fiber membrane under different conditions was measured by absorption spectra. The degradation efficiency of tetracycline between the composite fiber films and the other control groups is shown in Fig. 8a. It can be observed that the composite fiber membrane has the highest degradation efficiency of tetracycline under light conditions. The degradation efficiency was fast in the first 50 min, and it tended to be flat after 150 min. The degradation efficiency was almost unchanged, indicating that the degradation ability of the composite film reached the upper limit at this time. In summary, the degradation efficiency of composite fiber membrane for 10 $mg{\cdot}L^{-1}$ tetracycline solution can get 74%, which is better than that of most fiber membranes loaded with photocatalyst [62].

After proving that the composite fiber membrane possesses the ability to photocatalytic degradation tetracycline, the photocatalytic degradation ability of the composite fiber membrane loaded with different photocatalysts was compared. As shown in Fig. 8b, the degradation efficiencies of tetracycline by composite fiber membranes containing TiO_2, AgT, VT, and AgVT photocatalyst were compared. AgV group

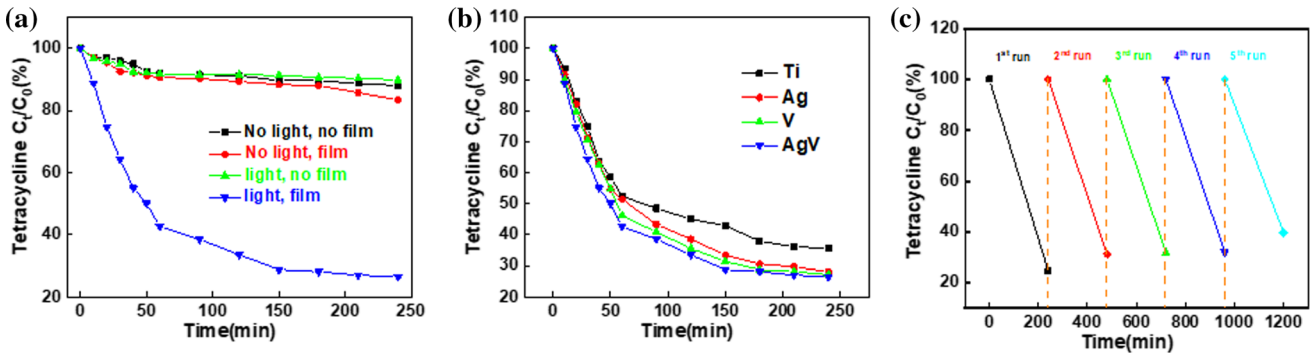

Figure 8 **a** Degradation efficiency of the composite film (AgVT) and control (without film) under light; **b** Photocatalytic degradation of tetracycline by different fiber membranes; **c** Cyclic degradation performance of different fiber membranes for photocatalytic degradation of tetracycline.

presented the highest photocatalytic degradation efficiency. The degradation efficiency of the TiO_2 group was the weakest compared with that of the TiO_2 group, which was also consistent with the activity experiment of the previous catalyst. Figure 8c exhibits the cyclic photocatalytic degradation ability of the composite fiber membrane. It can be seen that after five cycles, the degradation rate of tetracycline decreased slightly, but still maintained at a high level of 70% [63].

Conclusions

In this paper, the organic porous nanoparticles and inorganic photocatalysts were combined by electrospinning technology to prepare the composite nanofiber membrane with adsorption and photocatalytic effects for sewage treatment. With the metal doping, the visible light response is enhanced, the AgVT sample can degrade 10 mg·L^{-1} MB solution in 90 min under illumination completely. PVDF/PVP-NPs composite fiber membrane can adsorb and photocatalytic degrade MB. After five cycles, the degradation rate remained above 99%. Moreover, the degradation efficiency of PVDF/PVP-NPs composite fiber membrane in photocatalytic degradation of tetracycline is more than 74%, and the photocatalytic degradation efficiency remained at about 60% after five cycles. This work provides an attractive avenue for the construction of a photocatalytic membrane toward the efficient removal of dye and organic pollutants.

Acknowledgements

We acknowledge financial support from National Natural Science Foundation of China (51473048, 21603067, and 51773055) and Hubei Nature Science Foundation of China (2014CFB549 and 2019CFB748).

Author contributions

XC and BJ: Substantial contributions to the conception or design of work; PL and HR contribute equally to this work for carrying out the experiments and measurements. YP contributes to analysis, interpretation of data and draft writing. ZX and CL draft and revise the manuscript.

Declarations

Conflict of interest The authors declare that we have no financial interests or personal relationships that can inappropriately influence the work reported in this paper. We declare that there is no commercial or associative interest that represents a conflict of interest in connection with the work submitted.

Supplementary Information: The online version contains supplementary material available at https://doi.org/10.1007/s10853-023-08738-3.

References

[1] Anwer H, Mahmood A, Lee J, Kim K-H, Park J-W, Yip ACK (2019) Photocatalysts for degradation of dyes in industrial effluents: opportunities and challenges. Nano Res 12:955–972

[2] Li H, Liu S, Zhao J, Feng N (2016) Removal of reactive dyes from wastewater assisted with kaolin clay by magnesium hydroxide coagulation process. Colloids Surf A 494:222–227

[3] Hassan MM, Carr CM (2018) A critical review on recent advancements of the removal of reactive dyes from dyehouse effluent by ion-exchange adsorbents. Chemosphere 209:201–219

[4] Lyu W, Li JQ, Trchova M, Wang G, Liao YZ, Bober P, Stejskal J (2022) Fabrication of polyaniline/poly(vinyl alcohol)/montmorillonite hybrid aerogels toward efficient adsorption of organic dye pollutants. J Hazard Mater 435:129004. https://doi.org/10.1016/j.jhazmat.2022.129004

[5] Chen W, Mo J, Du X, Zhang Z, Zhang W (2019) Biomimetic dynamic membrane for aquatic dye removal. Water Res 151:243–251

[6] Lin QQ, Zeng GY, Luo GQ, Cheng XC, Zhao ZY, Li H (2021) Self-cleaning photocatalytic MXene composite membrane for synergistically enhanced water treatment: oil/water separation and dyes removal. Chem Eng J 427:131668

[7] Xiao J, Zhang J, Lv W, Song Y, Zheng Q (2017) Multifunctional graphene/poly(vinyl alcohol) aerogels: In situ hydrothermal preparation and applications in broad-spectrum adsorption for dyes and oils. Carbon 123:354–363

[8] Ai LH, Jiang J (2012) Removal of methylene blue from aqueous solution with self-assembled cylindrical graphene-carbon nanotube hybrid. Chem Eng J 192:156–163

[9] Yin J, Deng B (2015) Polymer-matrix nanocomposite membranes for water treatment. J Membr Sci 479:256–275

[10] Ye H, Zhang CL, Huo CW, Zhao BY, Zhou YH, Wu YC, Shi SP (2021) Advances in the application of polymers of intrinsic microporosity in liquid separation and purification: membrane separation and adsorption separation. Polym Rev 61(2):239–279

[11] Jin X-H, Price MB, Finnegan JR, Boott C (2018) Long-range exciton transport in conjugated polymer nanofibers prepared by seeded growth. Science 360:897–900

[12] Xue Z, Xiong Q, Zou C, Chi H, Ji Z (2020) Growth of carbon nanofibers through chemical vapor deposition for enhanced sodium ion storage. Mater Res Bull 133:111049. https://doi.org/10.1016/j.materresbull.2020.111049

[13] Liu S, Shan H, Xia S, Yan J, Ding B (2020) Polymer template synthesis of flexible SiO_2 nanofibers to upgrade composite electrolytes. ACS Appl Mater Interfaces 12:31439–31447

[14] Ahmed FE, Lalia BS, Hashaikeh R (2015) A review on electrospinning for membrane fabrication: challenges and applications. Desalination 356:15–30

[15] Jie YA, Tian BA, Yy B, Wc A, Long BA, Dong WA, Jl A, Mc A, Sqs C, Sh A (2022) Nanostructured superior oil-adsorbent nanofiber composites using one-step electrospinning of polyvinylidene fluoride/nanocellulose. Compos Sci Technol 224:109490. https://doi.org/10.1016/j.compscitech.2022.109490

[16] Beck RJ, Zhao Y, Fong H, Menkhaus TJ (2017) Electrospun lignin carbon nanofiber membranes with large pores for highly efficient adsorptive water treatment applications. J Water Process Eng 16:240–248

[17] Dorneanu PP, Cojocaru C, Olaru N, Samoila P, Airinei A, Sacarescu L (2017) Electrospun PVDF fibers and a novel PVDF/$CoFe_2O_4$ fibrous composite as nanostructured sorbent materials for oil spill cleanup. Appl Surf Sci 424:389–396

[18] Seraji AA, Aghvami-Panah M, Shams-Ghahfarokhi F (2022) Evaluation of ultimate engineering properties of polytetrafluoroethylene/carbon-aerogel/glass fiber porous composite. Colloids Surf A Physicochem Eng Asp 647:128975. https://doi.org/10.1016/j.colsurfa.2022.128975

[19] Li X, Fang X, Pang R, Li J, Sun X, Shen J, Han W, Wang L (2014) Self-assembly of TiO_2 nanoparticles around the pores of PES ultrafiltration membrane for mitigating organic fouling. J Membr Sci 467:226–235

[20] Liu X, Wang L, Zhou X, He X, Zhou M, Jia K, Liu X (2021) Design of polymer composite-based porous membrane for in-situ photocatalytic degradation of adsorbed organic dyes-ScienceDirect. J Phys Chem Solids 154:110094. https://doi.org/10.1016/j.jpcs.2021.110094

[21] Malato S, Fernández-ibáez P, Maldonado MI, Blanco J, Gernjak W (2009) Decontamination and disinfection of water by solar photocatalysis: recent overview and trends. Catal Today 147:1–59

[22] Deng L, Chandrasekaran S, Bowen C, Li Z, Zhang P, Yuan Q, Ren X (2018) Spinel photocatalysts for environmental remediation, hydrogen generation, CO_2 reduction and photoelectrochemical water splitting. J Mater Chem A 6:11078–11104

[23] Pivert ML, Kerivel O, Zerelli B, Leprince-Wang Y (2021) ZnO nanostructures based innovative photocatalytic road for air purification. J Clean Prod 318:128447. https://doi.org/10.1016/j.jclepro.2021.128447

[24] García-López E, Marcì G, Pomilla FR, Paganini MC, Gionco C, Giamello E, Palmisano L (2018) ZrO_2 based materials as photocatalysts for 2-propanol oxidation by using UV and solar light irradiation and tests for CO_2 reduction. Catal Today 313:100–105

[25] Yamen AS, Amer H, Jenny S, Bahnemann DW (2018) Co-Catalyst-free photocatalytic hydrogen evolution on TiO2: synthesis of optimized photocatalyst through statistical material science. Appl Catal B 238:422–433

[26] Jiang W, Li Z, Liu C, Wang D, Che G (2021) Enhanced visible-light-induced photocatalytic degradation of

tetracycline using BiOI/MIL-125(Ti) composite photocatalyst. J Alloys Compds 854:157166. https://doi.org/10.1016/j.jallcom.2020.157166

[27] Zheng H, Meng X, Chen J, Que M, Zhao Y (2021) In situ phase evolution of TiO_2/Ti_3C_2T heterojunction for enhancing adsorption and photocatalytic degradation. Appl Surf Sci 545:149031. https://doi.org/10.1016/j.apsusc.2021.149031

[28] Jiang XH, Duan YN, Tian Y, Chen M, Li MK, Liu HH, Yang WL, Tian MK (2022) Facile one-pot hydrothermal method to prepare Sn(II) and N co-doped TiO_2 photocatalyst for water splitting under visible light irradiation. Rare Met 41:406–414

[29] Huang H, He M, Yang X, Tian Z, Wen B (2019) One-pot hydrothermal synthesis of TiO_2/RCN heterojunction photocatalyst for production of hydrogen and rhodamine B degradation. Appl Surf Sci 493:202–211

[30] He Y, He Q, Liu Z, Wang O, Guli M (2019) Controllable preparation and improved performance of TiO2 photocatalysts with various structures. Mater Technol 35:1–10

[31] Iglesias O, Rivero MJ, Urtiaga AM, Ortiz I (2016) Membrane-based photocatalytic systems for process intensification. Chem Eng J 305:136–148

[32] Srisawang N, Chaiyasat A, Ngernchuklin P, Chaiyasat P (2020) Novel reusable pH-responsive photocatalyst polymeric microcapsules for dye treatment. Int J Energy Res 45:7535–7548

[33] Xu C, Shao F, Yi Z, Dong H, Dong L (2019) Highly chlorine resistance polyamide reverse osmosis membranes with oxidized graphitic carbon nitride by ontology doping method. Sep Purif Technol 223:178–185

[34] Long ZQ, Li QG, Wei T, Zhang GM, Ren ZJ (2020) Historical development and prospects of photocatalysts for pollutant removal in water. J Hazard Mater 395:122599. https://doi.org/10.1016/j.jhazmat.2020.122599

[35] Liao XL, Sun DX, Cao S, Zhang N, Huang T, Lei YZ, Wang Y (2021) Freely switchable super-hydrophobicity and super-hydrophilicity of sponge-like poly(vinylidene fluoride) porous fibers for highly efficient oil/water separation. J Hazard Mater 416:125926. https://doi.org/10.1016/j.jhazmat.2021.125926

[36] An AK, Guo J, Lee EJ, Jeong S, Zhao Y, Wang Z, Leiknes TO (2016) PDMS/PVDF hybrid electrospun membrane with superhydrophobic property and drop impact dynamics for dyeing wastewater treatment using membrane distillation. J Membr Sci 525:57–67

[37] Ning J, Yang M, Yang H, Xu Z (2016) Tailoring the morphologies of PVDF nanofibers by interfacial diffusion during coaxial electrospinning. Mater Des 109:264–269

[38] Daghrir R, Drogui P (2013) Tetracycline antibiotics in the environment: a review. Environ Chem Lett 11:209–227

[39] Pan Y, Xu Z, Tan W, Zhu Y, Wang Y, Li P, Chen X, Sun Z, Li C, Jiang B (2021) Novel amino-functionalized hypercrosslinked polymer nanoparticles constructed from commercial macromolecule polystyrene via a two-step strategy for CO_2 adsorption. New J Chem 44:21125–21133

[40] Du CX, Wang ZH, Liu GY, Wei W, Dan Y (2021) One-step electrospinning PVDF/PVP-TiO_2 hydrophilic nanofiber membrane with strong oil-Water separation and anti-fouling property. Colloids Surf A Physicochem Eng Asp 624:126790. https://doi.org/10.1016/j.colsurfa.2021.126790

[41] Dong C, Yuan X, He M, Yao K (2012) Preparation of PVA/PEI ultra-fine fibers and their composite membrane with PLA by electrospinning. J Biomater Sci Polym Ed 17:631–643

[42] Wang T, Yao H, Song N, Yang Y, Shi K, Guan S (2021) Microporous polymer networks constructed from cross-linkable linear polyimides for CO2 adsorption. Micropor Mesopor Mater 311:110708. https://doi.org/10.1016/j.micromeso.2020.110708

[43] Xu F, Tan H, Fan J, Cheng B, Yu J, Xu J (2021) Electrospun TiO_2-based photocatalysts. Solar RRL 5:2000571

[44] Chang LH, Cho CP (2018) Enhanced photocatalytic characteristics by Ag-sensitized TiO_2 photocatalysts with mixed phases. Mater Chem Phys 223:683–693

[45] Lv T, Zhao J, Chen M, Shen K, Zhang D, Jin Z, Zhang G, Liu Q (2018) Boosted visible-light photodegradation of methylene blue by V and Co Co-doped TiO_2. Materials 11:1946. https://doi.org/10.3390/ma11101946

[46] Matiullah K, Song YT, Chen N, Cao WB (2013) Effect of V doping concentration on the electronic structure, optical and photocatalytic properties of nano-sized V-doped anatase TiO_2. Mater Chem Phys 142:148–153

[47] Saliby IE, Erdei L, Shon HK, Kim JH (2011) Development of visible light sensitive titania photocatalysts by combined nitrogen and silver doping. J Ind Eng Chem 17:358–363

[48] Li Y, Ma M, Chen W, Li L, Zen M (2011) Preparation of Ag-doped TiO_2 nanoparticles by a miniemulsion method and their photoactivity in visible light illuminations. Mater Chem Phys 129(12):501–505

[49] Jakob M, Levanon H, Kamat PV (2003) Charge distribution between UV-irradiated TiO_2 and gold nanoparticles: determination of shift in the fermi level. Nano Lett 3:353–358

[50] Liu Y, Song L, Du L, Gao P, Xu X (2020) Preparation of polyaniline/emulsion microsphere composite for efficient adsorption of organic dyes. Polymers 12:167. https://doi.org/10.3390/polym12010167

[51] Yang G, Huang Q, Gan D, Huang H, Wei Y (2019) Biomimetic functionalization of carbon nanotubes with poly(-ionic liquids) for highly efficient adsorption of organic dyes.

J Mol Liq 296:112059. https://doi.org/10.1016/j.molliq.2019.112059

[52] Ho YS, Mckay G (1998) Sorption of dye from aqueous solution by peat. Chem Eng J 70:115–124

[53] Zhuang Y, Zhu Q, Li GZ, Wang ZL, Zhan P, Ren C, Si ZH, Li SF, Cai D, Qin PY (2022) Photocatalytic degradation of organic dyes using covalent triazine-based framework. Mater Res Bull 146:111619. https://doi.org/10.1016/j.materresbull.2021.111619

[54] Zhang YB, Tan HB, Wang CF, Li BW, Yang H, Hou HT, Xiao CF (2022) TiO_2-coated glass hollow fiber membranes: preparation and application for photocatalytic methylene blue removal. J Eur Ceram Soc 42:2496–2504

[55] Yna D, Kyb C, Fxb C, Wz B, Qzb C, Ke L, Kya D, Dong W (2019) Synergistic effect on TiO_2 doped poly (vinyl alcohol-co-ethylene) nanofibrous film for filtration and photocatalytic degradation of methylene blue, Composites. Communications 12:112–116

[56] Zhang D, Dai F, Zhang P, An Z, Zhao Y, Chen L (2019) The photodegradation of methylene blue in water with PVDF/GO/ZnO composite membrane. Mater Sci Eng 96:684–692

[57] Wang Y, Zhu L, Wang M, Zhang M, Yang Y, Zhu Q, Lei Y (2016) Microstructure and photocatalytic activity of porous TiO_2–Fe_2O_3 composite film by PEO coupled with post heat treatment. Int J Hydrog Energy 41:15703–15709

[58] Pascariu P, Cojocaru C, Samoila P, Olaru N, Airinei A (2021) Novel electrospun membranes based on PVDF fibers embedding lanthanide doped ZnO for adsorption and photocatalytic degradation of dye organic pollutants. Mater Res Bull 141:111376. https://doi.org/10.1016/j.materresbull.2021.111376

[59] Chen X, Nie Q, Shao Y, Wang Z, Cai Z (2021) TiO_2 nanoparticles functionalized borneol-based polymer films with enhanced photocatalytic and antibacterial performances. Environ Technol Innov 21:101304. https://doi.org/10.1016/j.eti.2020.101304

[60] Xue Y, Chang Q, Hu X, Cai J, Yang H (2020) A simple strategy for selective photocatalysis degradation of organic dyes through selective adsorption enrichment by using a complex film of CdS and carboxylmethyl starch. J Environ Manag 274:111184. https://doi.org/10.1016/j.jenvman.2020.111184

[61] Jalali K, Pajootan E, Bahrami H (2019) Elimination of hazardous methylene blue from contaminated solutions by electrochemically magnetized graphene oxide as a recyclable adsorbent. Adv Powder Technol 30:2352–2362

[62] Chen W, Liu J, An J, Wang L, Zhu Y, Sillanpää M (2018) Continuous removal of tetracycline in a photocatalytic membrane reactor (PMR) with $ZnIn_2S_4$ as adsorption and photocatalytic coating layer on PVDF membrane. J Photochem Photobiol A Chem 364:732–739

[63] Obregon S, Hernandez-Uresti DB, Vazquez A, Sanchez-Martinez D (2018) Electrophoretic deposition of $PbMoO_4$ nanoparticles for photocatalytic degradation of tetracycline. Appl Surf Sci 457:501–507